In Situ Raman Spectroscopy of Lanthanum-Strontium-Cobaltite Thin Films

by
Justin Daniel Breucop
Candidate for Bachelor of Science in Materials Science and Engineering

Submitted to the
Department of Materials Science and Engineering
at the
Massachusetts Institute of Technology
May 2012

Signature of Author ....

Certified by ....
Yang Shao-Horn
Gail E. Kendall Chair in Mechanical Engineering
Associate Professor of Materials Science and Engineering
Thesis Advisor

Accepted by ....
Jeffrey Grossman
Carl Richard Soderberg Associate Professor of Power Engineering
Chairman, Undergraduate Thesis Committee

In Situ Raman Spectroscopy of Lanthanum-Strontium-Cobaltite Thin Films

by
Justin Daniel Breucop

Submitted to the
Department of Materials Science and Engineering
at the
Massachusetts Institute of Technology
May 2012

Abstract

Raman spectroscopy is used to probe the structural change of Lanthanum Strontium Cobaltite ($La_{1-x}Sr_xCoO_{3-\delta}$) thin films across change in composition (0%-60% strontium) and temperature (30°C-520°C). Raman shift peaks were identified and correlated with specific vibrational modes. Results were consistent with relevant data, but no transition to the high spin state was observed above 200°C. Compositions were compared to oxygen catalytic data to investigate success in high temperature electrochemical applications. No structural phase changes were found in the research of this thesis, interesting effects in the surface regime were observed and possible explanations are offered. Future research should focus on resolving the surface regime via altered experimental set up.

Keywords: LSC, LCO, Raman, *in situ*

1.0 Introduction and Background

This thesis seeks to investigate the relations between structural changes of perovskite Lanthanum-Strontium-Cobaltite ($La_{1-x}Sr_xCoO_{3-\delta}$ or LSC). LSC is a promising material for oxygen catalysis at intermediate temperatures of 500°C, applicable to solid oxide fuel cell technology as well as electrochemical cells for water splitting due to its reversibility. Through the use of Raman scattering spectroscopy, structural phases can be investigated in solid oxide fuel cell operating conditions. While no structural phase changes were found in the research of this thesis, interesting effects in the surface regime were found and possible explanations are offered.

1.1 Solid Oxide Fuel Cells

A solid oxide fuel cell (SOFC) is a device that converts chemical energy to electrical energy by oxidizing a fuel, typically hydrogen gas. SOFCs operate at a temperature ranging typically from 650°C – 1000°C and consist of a solid, nonporous metal oxide that conducts oxygen ions. The electrochemistry itself is very straightforward; the concept of a SOFC was around for about half a century, even before the capability to implement them existed. The problems lie in the effective region of the cathodic reaction and the high operating temperature.

The effective region over which the steps of the cathodic reaction is called the Triple Phase Boundary (TPB). This parameter is given as an effective length and the longer it is, the greater the effective surface area for the cathodic reaction to occur is.[1] While the exact reactions occurring are debated, the reduction of oxygen at the cathode involves two major steps:

$$O_2 \leftrightarrow 2O_{\text{ads}}$$

and

$$O_{ads} + 2e^- + V_O^{\bullet\bullet} \leftrightarrow O_O^x$$

where O_{ads} represents adsorbed oxygen on the surgace and other symbols follow standard Kroeger-Vink notation.[2] These steps show the catalysis of oxygen, which becomes the rate limiting reaction as temperature decreases and is referred to as the Oxygen Reduction Reaction (ORR). The kinetics of the ORR are determined through the electrical surface exchange coefficient, k^q.[3,4]

1.2 Perovskites

The greatest problem facing SOFCs currently is the high operating temperature: it limits the anode, electrolyte and cathode materials by forcing them to have very similar thermal expansion coefficients and, due to the high temperatures and corrosive conditions on the anodic side, requires the interconnects to have either expensive coatings or be made out of exotic, electron-conducting ceramics. Lower operating temperatures of about 550°C would allow for the use of cheaper materials to withstand the fuel cell environment. These "intermediate-temperature" solid oxide fuel cells can be made if a cathode material with a sufficiently high k^q is found. This search for faster ORR kinetics has led a large amount of research to investigating perovskites as possible materials.[5]

Perovskites are ceramics with an ABO3 chemical composition. As a material, a variety of them they have a wide range of interesting properties. Some perovskites exhibit piezoelectric characteristics and others exhibit superconductivity at low temperatures.[6] Of particular interest to fuel cells and electrocatalysis, many perovskites exhibit excellent catalytic properties and are commonly investigated as new possible cathode materials.

One promising class of perovskites are Mixed Ionic Electronic Conductors (MIEC).[7] They allow for oxygen ion diffusion and electron mobility, increasing the conceptual TPB to allow any region on the cathode to allow for oxygen reduction. They exhibit high ORR activity as well.[1,3] Within this class, Lanthanum Cobaltite ($LaCoO_3$) has shown some previous success as a cathode material. It has an R-3c crystal structure, which is part of a unique set of space groups that are described by both hexagonal and rhombohedral lattice systems.[8] Improvements on LCO_3 have been found by adding strontium. Added strontium increases the non-stoichiometry of the material and pushes the crystal structure to a very symmetric Pm-3m space group.[9] These symmetries can be investigated *in situ* using Raman spectroscopy, which will be introduced in the next section.

1.3 Raman Scattering Theory

Photon scattering usually occurs elastically (Rayleigh scattering) but a small fraction of scattered photons are scattered inelastically. The inelastic scattering of light is Raman scattering. Scattered photons have an energy either higher or lower than the incident photon and this difference is proportional to phonon energies in the material.[10] The phonon interaction changes the electron energy state by locally displacing the atoms of the material, distorting the dipole moment the electron experiences. The small number of Raman scattered photons can be used to develop a Raman spectrum, whose peaks illuminate bulk and surface structure information.

Here, a classical representation of Raman scattering will be sufficient. The quantum treatment only adds the explanation of rotational Raman active modes. In both treatments, the origin of Raman scattered radiation arises from the oscillating electric dipole moments induced in a material system by the electromagnetic fields of the incident light.[11] The origin of Raman scattering comes from the frequency dependent linear induced electric dipole vectors **p**, given by

$$\boldsymbol{p} = \boldsymbol{\alpha} \cdot \boldsymbol{E} \tag{1}$$

where E is the electric field vector of the incident radiation and **α** is the polarizability tensor of the material system. The polarizability tensor is a function of the nuclear coordinates and by extension the vibrational frequencies of the material. To derive the relation between the polarizability tensor and material properties, consider a simple on molecule system, free to vibrate but not rotate. The frequency contribution through molecular vibration can be found though a Taylor expansion of α_{ij}, a component of **α**, with respect to the normal coordinates of the vibration, yielding

$$\alpha_{ij} = \left(\alpha_{ij}\right)_0 + \sum_k \left(\frac{\partial \alpha_{ij}}{\partial Q_k}\right)_0 Q_k + \frac{1}{2}\sum_{k,l}\left(\frac{\partial^2 \alpha}{\partial Q_k \partial Q_l}\right)_0 Q_k Q_l \cdots \tag{2}$$

$\left(\alpha_{ij}\right)_0$ is the initial value of α_{ij} at equilibrium configuration, Q_k, $Q_l\cdots$ are normal coordinates of vibration associated with the molecular vibrational frequencies ω_k, ω_l, $\cdots$, summed over all normal coordinates. The derivatives are to be taken at the equilibrium configuration. Ignoring terms that involve Q above the first power, eq. (2) can be written as

$$\left(\alpha_{ij}\right)_k = \left(\alpha_{ij}\right)_0 + \left(\alpha'_{ij}\right)_k Q_k \tag{3}$$

where

$$\left(\alpha'_{ij}\right)_k = \left(\frac{\partial \alpha_{ij}}{\partial Q_k}\right)_0 \tag{4}$$

$(\alpha'_{ij})_k$ are components of a derived polarizability tensor, $\boldsymbol{\alpha}'_k$, derived with respect to normal coordinate Q_k. This holds true for all components of $\boldsymbol{\alpha}'_k$. Assuming simple harmonic motion for the molecular vibrations, Q_k has a sinusoidal time dependence and $\boldsymbol{\alpha}'_k$ can be written as

$$\boldsymbol{\alpha}_k = \boldsymbol{\alpha}_0 + \boldsymbol{\alpha}'_k Q_{k0} \cos(\omega_k t + \delta_k) \tag{5}$$

where Q_{k0} is the normal coordinate amplitude and δ_k is a phase factor. The frequency dependence of $\boldsymbol{E}$ is given by

$$\boldsymbol{E} = \boldsymbol{E}_0 \cos(\omega_1 t) \tag{6}$$

where ω_1 is the frequency of the incoming light. When combined with eq. (1) and eq. (5), the full induced dipole moment is obtained

$$\boldsymbol{p} = \boldsymbol{\alpha}_0 \boldsymbol{E}_0 \cos(\omega_1 t + \delta) + \boldsymbol{\alpha}'_k \boldsymbol{E}_0 Q_{k0} \cos(\omega_k t + \delta) cos(\omega_1 t) \tag{7}$$

which can be rewritten using the cosine product trigonometric identity as

$$\boldsymbol{p} = \boldsymbol{p}(\omega_1) + \boldsymbol{p}(\omega_1 - \omega_k) + \boldsymbol{p}(\omega_1 + \omega_k) \tag{8}$$

where

$$\boldsymbol{p}(\omega_1) = \boldsymbol{\alpha}_0 \cdot \mathbf{E}_0 \cos(\omega_1 t) \tag{9}$$

corresponds to Rayleigh scattering and

$$\boldsymbol{p}(\omega_1 \pm \omega_k) = \boldsymbol{\alpha}_k^{Ram} \cdot \boldsymbol{E}_0 \cos(\omega_1 t \pm \omega_k t \pm \delta_k) \tag{10}$$

Also

$$\boldsymbol{\alpha}_k^{\mathrm{Ram}} = \frac{1}{2}\boldsymbol{\alpha}'_k Q_k \tag{11}$$

with $\boldsymbol{\alpha}_k^{\mathrm{Ram}}$ representing the Raman polarizability tensor for vibrational normal coordinate k. The second term of eq. (8) corresponds to a decrease in frequency of scattered light, termed Stokes frequency, and the third corresponds to an increase, termed Anti-Stokes frequency. From eq. (11), there must be non-zero components of the Raman polarizability tensor, which is dependent on the derivative of the polarizability with respect to the normal coordinate at equilibrium condition, for Raman scattering to occur. This classical treatment of Raman scattering demonstrates qualitative selection rules for Raman scattering: it is dependent on the symmetry of the structure and the symmetry of the vibration elements. This extends to rotational modes through the quantum analysis, the explanation of which is formally similar to the discussion of classical induced dipole moments in the material.

A strong determinant of symmetries within LSC perovskites is the spin state of the material, which is caused by spin state transitions.$_{12}$ Crystal Field theory explains that low spin states are when electrons occupying transition metal orbitals are arranged according to the Aufbau principle due to large energy orbital splitting and higher spin states are caused by a lattice distortion from variation in transition metal valency, leading to small energy orbital splitting. High spin states correspond to electrons all having the same spin at each energy level, forgoing the Aufbau principle because the orbital energies are so close that Hund's rule of exclusion is used. Spin state transitions are also temperature dependent. Crystal Field theory explains lattice structure transitions and several are noticed in $LaCoO_3$., as several researchers demonstrate.[13] These transitions are where Raman spectroscopy is at its most powerful, since subtle structure changes have a profound effect on symmetries. Also, low laser penetration depth on LSC makes effects from the base layer of yttrium-stabilized zirconia (YSZ) and gadolinium doped ceria (GDC).

1.4 Raman Spectroscopy and Current Research

Raman spectroscopy plots the Raman scattering as offset from incident wavelength, in wavenumbers, vs. intensity of the response. The resulting spectra shows peaks at energy levels equivalent to the frequency of the energy of the associated vibrational mode. These peaks have a dependency on the crystal and vibrational symmetry as stated previously and the incident angle of light, if polarized, according to:

$$I = \frac{\pi^2 c_0}{2\varepsilon_0} \tilde{v}_s^4 p_0^2 \sin^2 \theta \qquad (12)$$

where I is the intensity or time-averaged power per unit solid angle, $p_0$is the amplitude of the induced electric dipole with the wavenumber $\tilde{v}_s$, and θ is the angle made by the incident radiation and the axis of the induced dipole. The peaks are also associated with defined, Raman-active modes.

These modes can be classified as wither internal modes that involve only the atoms of a molecular unit of oxygen octahedra while external modes correlate with vibrations between the larger molecular units, such as A site atoms. If the crystal symmetry and Wyckoff positions are known for the material, the Raman active internal and external modes can be determined. For R-3c, the $LCoO_3$ space group, with Wyckoff positions at 18e, 6b and 6a, there are five associated Raman active modes, outlined in Fig. 1a. In contrast, Pm-3m, a cubic system has no Raman active modes for Wyckoff positions 3d, 1b and 1a.[14]

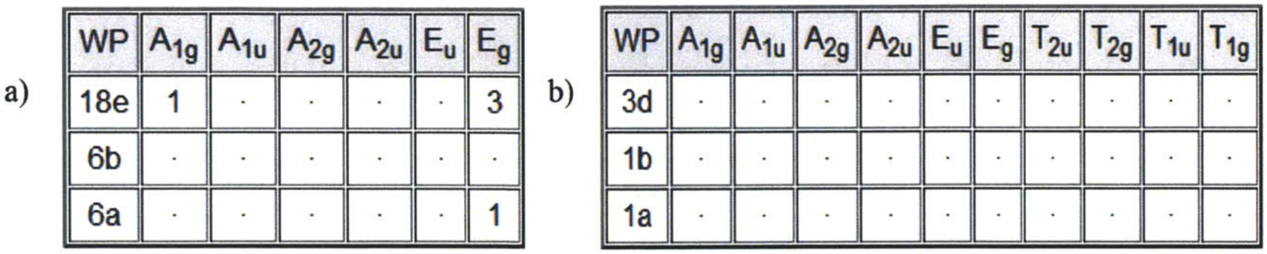

a)

WP	A_{1g}	A_{1u}	A_{2g}	A_{2u}	E_u	E_g
18e	1	·	·	·	·	3
6b	·	·	·	·	·	·
6a	·	·	·	·	·	1

b)

WP	A_{1g}	A_{1u}	A_{2g}	A_{2u}	E_u	E_g	T_{2u}	T_{2g}	T_{1u}	T_{1g}
3d	·	·	·	·	·	·	·	·	·	·
1b	·	·	·	·	·	·	·	·	·	·
1a	·	·	·	·	·	·	·	·	·	·

Fig. 1 Raman active modes for a) R-3c and b) Pm-3m.[14]

Research on SOFC cathode materials at intermediate temperatures is broad and can be investigated through several reviews cited here.[15,16,17] However, more relevant research regarding LSC and Raman spectroscopy will be summarized here. At the time of writing, there are no Raman studies of LSC above 250°C. *In situ* surface analysis of MIEC perovskite structures has been carried out to analyze cathode poisoning kinetics.[18] But Raman studies of *in situ* LSC cathodes have not. X-ray photon spectroscopy is one of the only methods used *in situ* to analyze cathodic thin films but results only lead to hypotheses of mechanistic interactions.[2]

Base spectra of YSZ and GDC have been found with peaks at 463 cm^{-1} for GDC and 620 cm^{-1} for YSZ. Ishikawa et al. have created Raman spectra ranging from 5 K to 300 K (room temperature).[19] The resulting spectra (Fig. 2) show spin state transitions from low to intermediate above about 80 K. Lattice dynamic calculations have also been carried out to identify Raman modes and have been compared to experimental data.[20] High intensity incident lasers have been shown to cause a background effect in Raman spectra of $LaCoO_3$, theorized to be due to surface heating. This is commonly associated with the semiconductor-metal transition associated with high spin state transitions at 500 K. In general, Raman studies of crystal structure for ceramic oxides involve Raman modes below 1500 cm^{-1}, while above that are surface effects on your sample.[21]

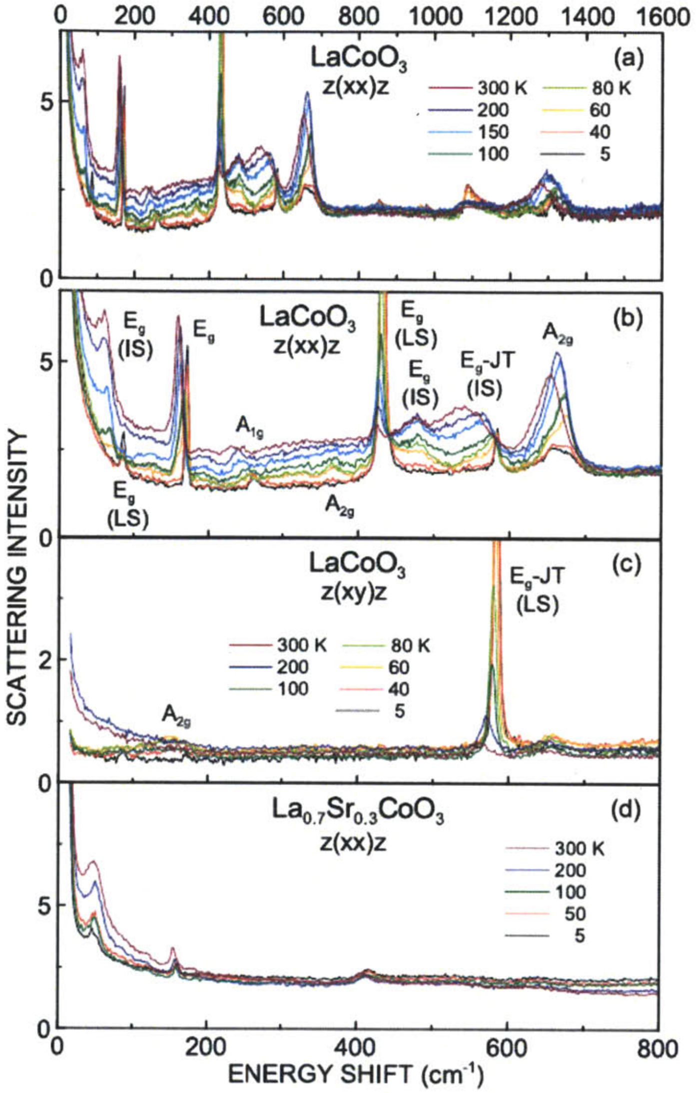

Fig. 2 Raman spectra for $LaCoO_3$ and $La_{0.7}Sr_{0.3}CoO_3$ at temperatures ranging from 5 to 300 K. Allowed Raman modes are shown at 172 cm-1, 261 cm-1, 432 cm^{-1}, and 584 cm^{-1}.

An important cross compositional takeaway of LSC is that there is a dampening of Raman signal as Sr concentration increases. This shows the shift to the cubic Pm-3m structure with no Raman active modes. The other important factor is that structural modes that don't experience a phase change show a leftward shift with temperature of around 15 cm^{-1} due to thermal expansion.[19]

2.0 Experimental

2.1 LSC Sample Preparation

LSC samples were synthesized using pulsed laser deposition (PLD) at Oak Ridge National Laboratories similarly to this lab's previous methods.$_{3,4}$ Thin films were composed of a single crystalline (001)-oriented yttria-stabilized zirconia (YSZ, Y_2O_3-stabilized ZrO_2) electrolyte (Princeton Scientific), a ≈4 nm thick layer of gadolinium-doped ceria, and a ≈140 nm thick layer of LSC at varying compositions. Details of PLD process follow.

The $Gd_{0.2}Ce_{0.8}O_2$ powder was synthesized via the Pechini method: Gd(NO3)3 and Ce(NO3)3 were dissolved into de-ionized water, ethylene glycol, and citric acid (Sigma-Aldrich). After esterification at about 100 °C, the resin was charred at 400 °C and then calcinated at 800 °C for 1 hour in air. The La0.8Sr0.2CoO3-δ (LSC) powder was synthesized using solid state reaction from a stoichiometric mixture of La2O3, SrCO3, and Co3O4 (Alfa Aesar) calcinated at 1000 °C for 12 hours in air. The PLD targets with a diameter of 25 mm were subsequently formed by uniaxial pressing at 50 MPa and sintered at 1350 °C for 20 hours in air.

YSZ, at 8 mol% yttrium oxide, single crystalline substrates with (001)-orientation, dimensions 10 x 5 x 0.5 mm, and one-sided polished (surface roughness < 1 nm) (Princeton Scientific) were used as PLD substrates. The GDC and LSC oxide films were deposited by PLD using a KrF excimer laser with $\lambda = 248$ nm, $f = 10$ Hz pulse rate, and $E \approx 50$ mJ pulse energy under $p(O_2)$ of 10 mTorr with 500 pulses of GDC at 550 °C, followed by $N = 15000$ pulses of LSC at 650 °C. After the deposition, the samples were cooled to room temperature within the PLD chamber at ≈ 10 mTorr. Samples were stored in a dry, air-tight container.

2.2 Procedure

The Raman spectrometer (Horiba, LabRAM HR) was calibrated to Silicon with 633 nm red laser light. Samples were mounted on the heat stage and set up to a flow of Argon with 10% Oxygen. Heating stage surface was calibrated using a thermocouple, applying a silver paste to the probe and sample surface to ensure good thermal contact. A temperature difference of 10°C (± 3°C) was found (see Appendix A). Raman spectra were collected on coarse 1800 grating to collect a wide range of data. Acquisition times used were 120s and 5 cycles for each section of the data, all on a D03 filter, which reduces intensity of detected signal by $10^{0.3}$ compared to unfiltered, enough to reduce most of the noise while maintaining peak definition. Data collection was also limited to Stokes radiation. Anti-Stokes measurements require much more sensitive equipment.

Measurements were taken at room temperature, 220°C, 370°C, and 520°C, holding at the temperature for 10 minutes before starting acquisition. To investigate thermal reversibility in material transitions, a second spectrum at room temperature was collected for the pure Lanthanum. Some measurements at 520°C saturated the detector, so a D06 filter was used, resulting in an intensity offset from D03 by $10^{0.3}$. Data shown has been calibrated to D03 filter, 120s acquisition times, with some offset to allow for easier viewing of data.

Data was collected over the range of 50 to 3800 cm^{-1}. This range was chosen to capture as much information as possible since this is a novel endeavor with LSC and MIECs in general. Results from 1200 to 2000 cm^{-1} were omitted in scans of intermediate composition materials (Sr = 0.2, 0.4) due to lack of any non-background Raman response in that region. Material compositions past 60% strontium were not chosen due to loss of catalytic properties due to divergence from perovskite structure.

3.0 Results and Discussion

Raman spectroscopy is a highly sensitive technique susceptible to background noise from other photonic interactions in the material. There are other types of responses that can be detected such as fluorescence interference. Most of our uncertainty lies in the high Raman shift regime above 2000 cm^{-1}. Different filters were used to avoid detector saturation and the relative intensities are slightly skewed as a result. Spectra have several points of discontinuity due to spectrometer range and were pieced together after. The effect isn't noticeable except between sections run on different filters, around 3000 cm-1 on samples. These points were omitted as possible peaks in discussion. Another source of error in our technique is that the crystallographic orientation of the sample wasn't consistent across sample compositions. Calibration between acquisition runs also led to a variation in Raman peak of samples within 5 cm-1. To better show details, results were split into two regimes. Complete spectra provided in Appendix B.

3.1 Spectra figures and peaks - Structure Regime

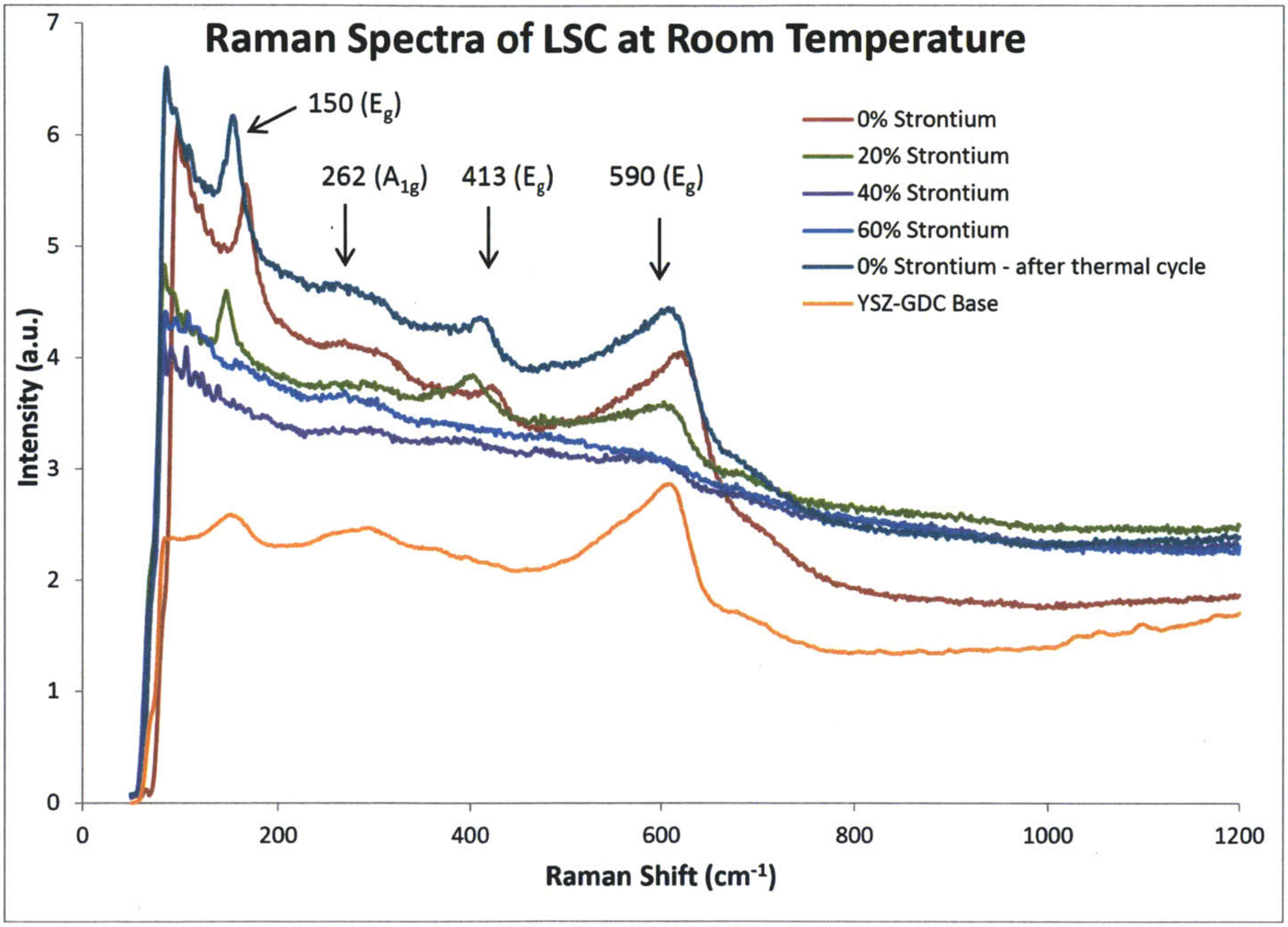

Fig. 3 Collected spectra of LSC and YSZ-GDC base at room temperature for Raman Shift below 1200 cm^{-1}. Identified Raman peaks are labeled. Eg mode associated with first Raman peak is not clearly discernible. Post cycle reproduction of spectra shows thermal reversibility.

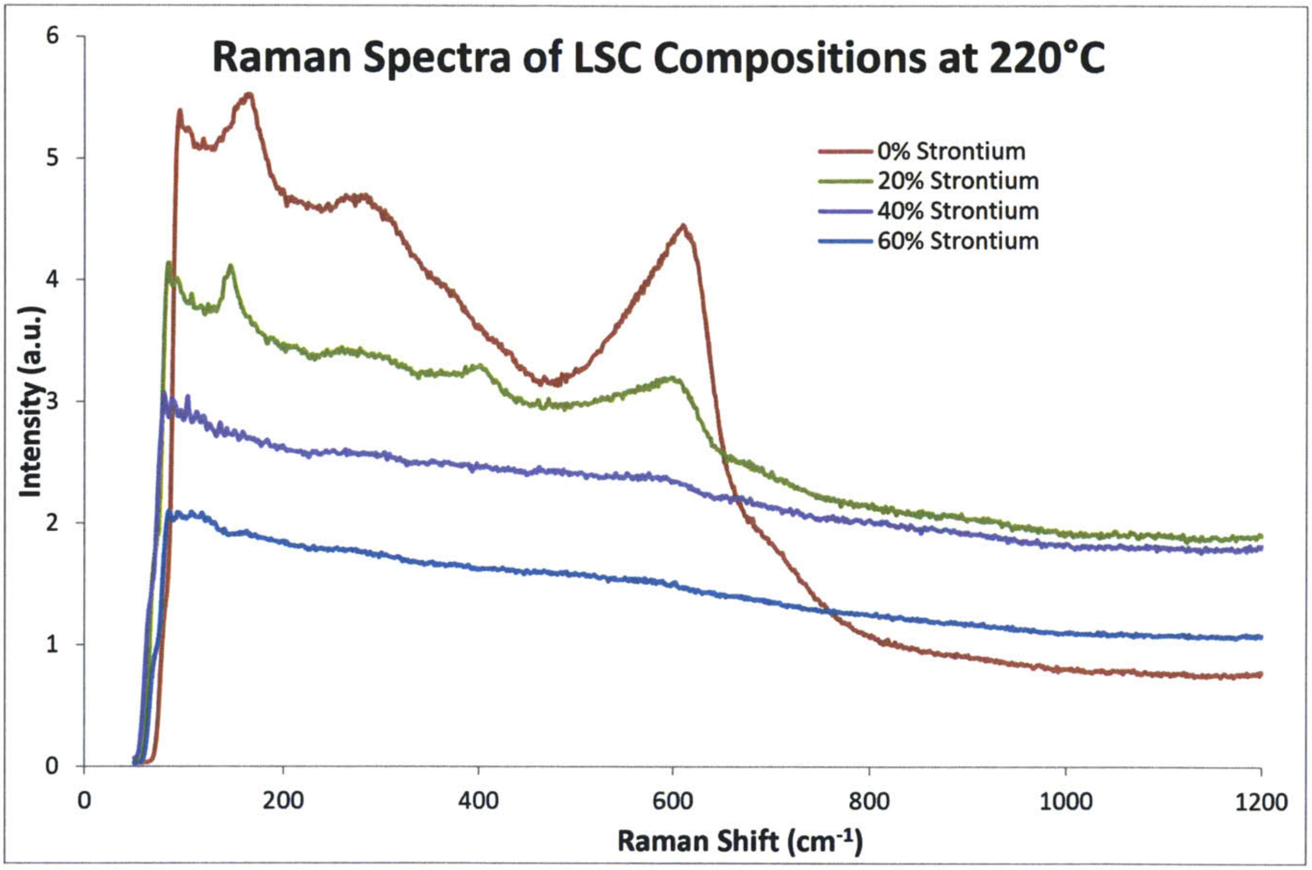

Fig. 4 Collected spectra at 220°C for 0% to 60% strontium compositions of LSC below 1200 cm^{-1}. Peaks for 40% and 60% are difficult to discern but arguments can be made for 260 cm^{-1} and 50 cm^{-1}.

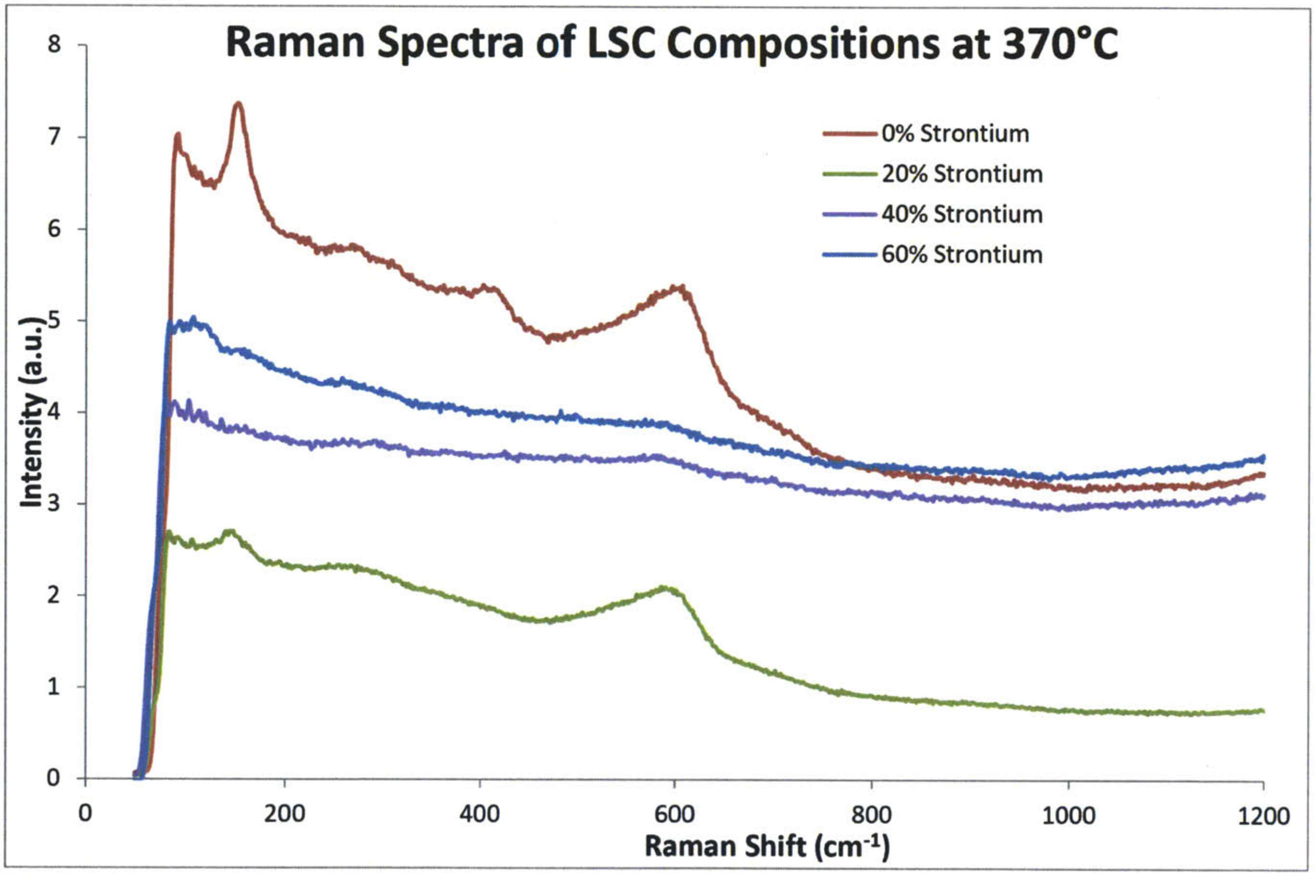

Fig. 5 Collected spectra at 370°C for 0% to 60% strontium compositions of LSC below 1200 cm^{-1}. Note disappearance of 413 cm^{-1} E_g peak in 20% when compared to 220°C spectra.

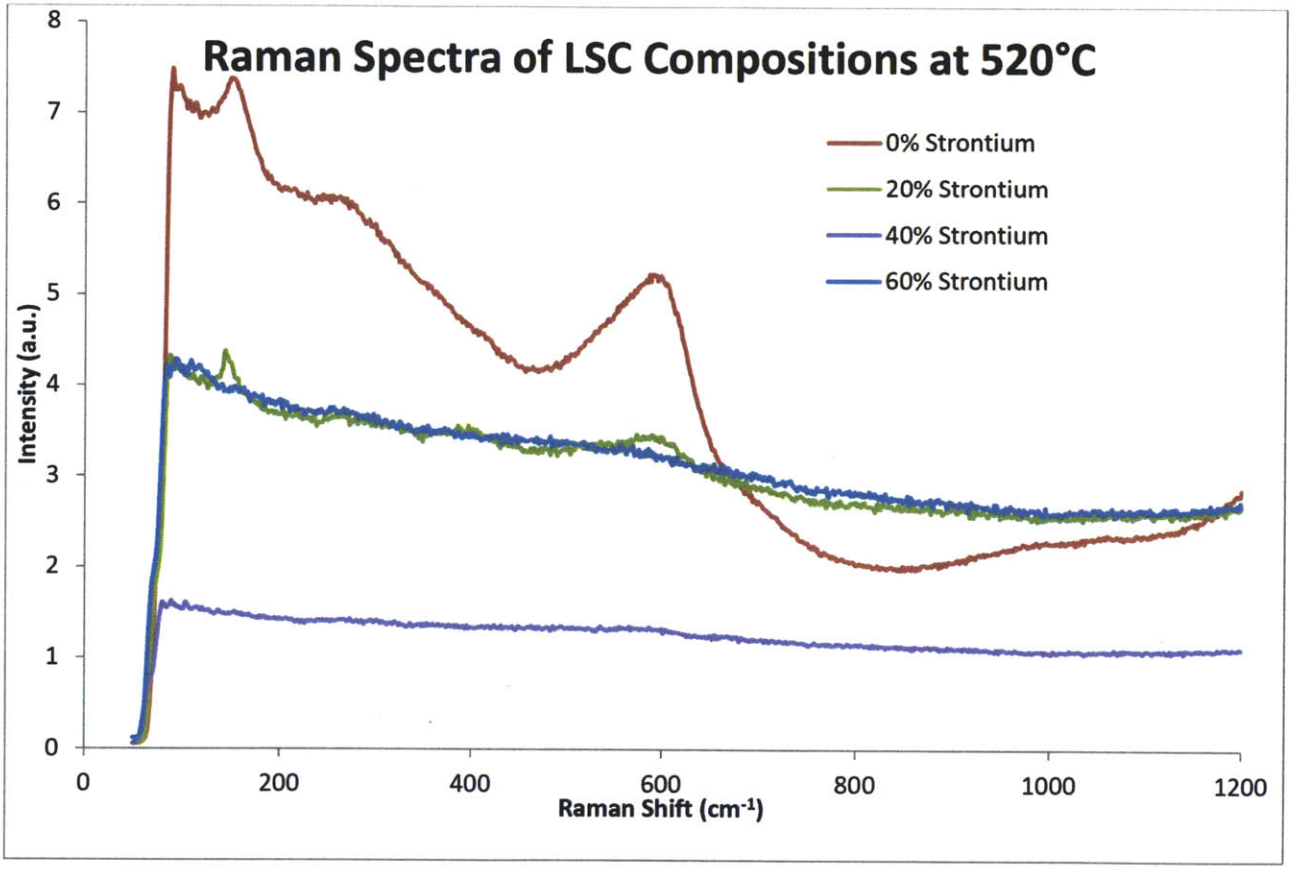

Fig. 6 Collected spectra at 520°C for 0% to 60% strontium compositions of LSC below 1200 cm^{-1}.
No peaks observed in 60% composition.

3.2 Discussion – Structure Regime

In Raman spectra, modes associated with the crystal lattice (below 1500 cm^{-1}) demonstrated a slight shift to lower wavenumbers, matching theory of crystal vibrational energy: thermal expansion leads to larger bond lengths, lower stiffness and thus lower energy Raman scattering. Our YSZ base in Fig. 3 showed Raman responses lower than expected values from Abernathy (253 cm^{-1} vs 463 cm^{-1} and 587 cm^{-1} vs 620 cm^{-1}).$_{22}$ But compared to the base, structural responses of LSC are damped with increasing strontium concentration in all figures (3-6), consistent with our expectations as the crystal structure becomes more cubic. Once lanthanum substitution reaches 60% strontium, the ceramic is mostly Pm-3m, with no active Raman modes. The damping of the peaks indicates that these results, also consistent with Raman data on $LCoO_3$, are not strongly influenced by the YSZ-GDC base. Raman peaks were assigned and matched with their associated vibrational modes.

No phase transition was seen with temperature. The high spin state transition that was reported to occur at 500 K (226°C) was not seen. There was a sharp increase in background on 520°C, D03 filter that was consistent with the reported semiconductor-metal transition (rapid increase in background with increasing Raman shift) but the temperature was already well past the reported transition. This could demonstrate that the transition is not as much a function of temperature as previously thought and should be investigated further. The laser may have an unpredicted effect on this sharp background increase. The background effect is however reversible.

Lastly, the 413 peak, associated with the internal mode of oxygen bending, Eg 432, does not always appear in spectra. Samples were left at their orientation across temperature runs, so the appearance, disappearance and reappearance of the peak (0% strontium in Fig 3, 4, and 5) are due to uncertain effects since orientation of samples between temperature measurements was maintained.

3.3 Spectra figures and peaks – Surface Regime

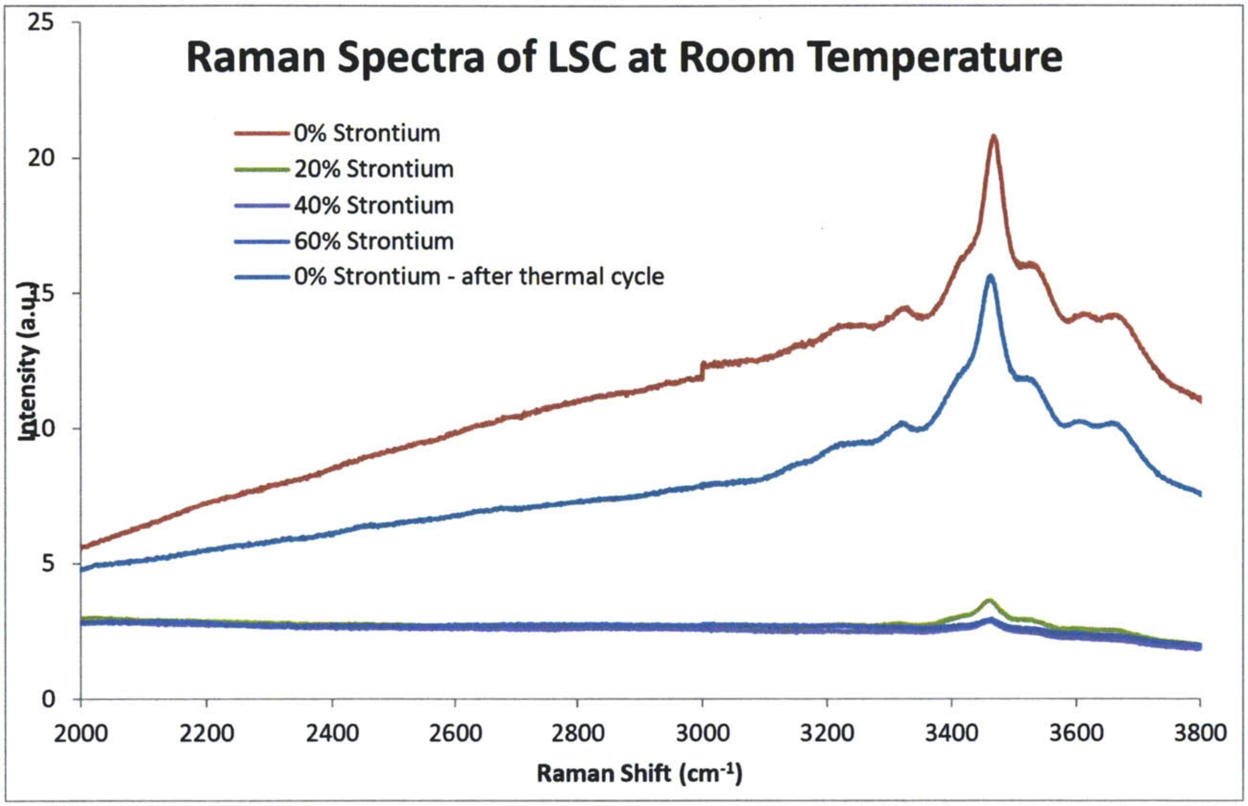

Fig. 7 Collected spectra at room temperature for 0% to 60% strontium compositions of LSC above 2000 cm^{-1}. Discontinuity at 3000 cm^{-1} is an experimental artifact from acquisition window stitching.

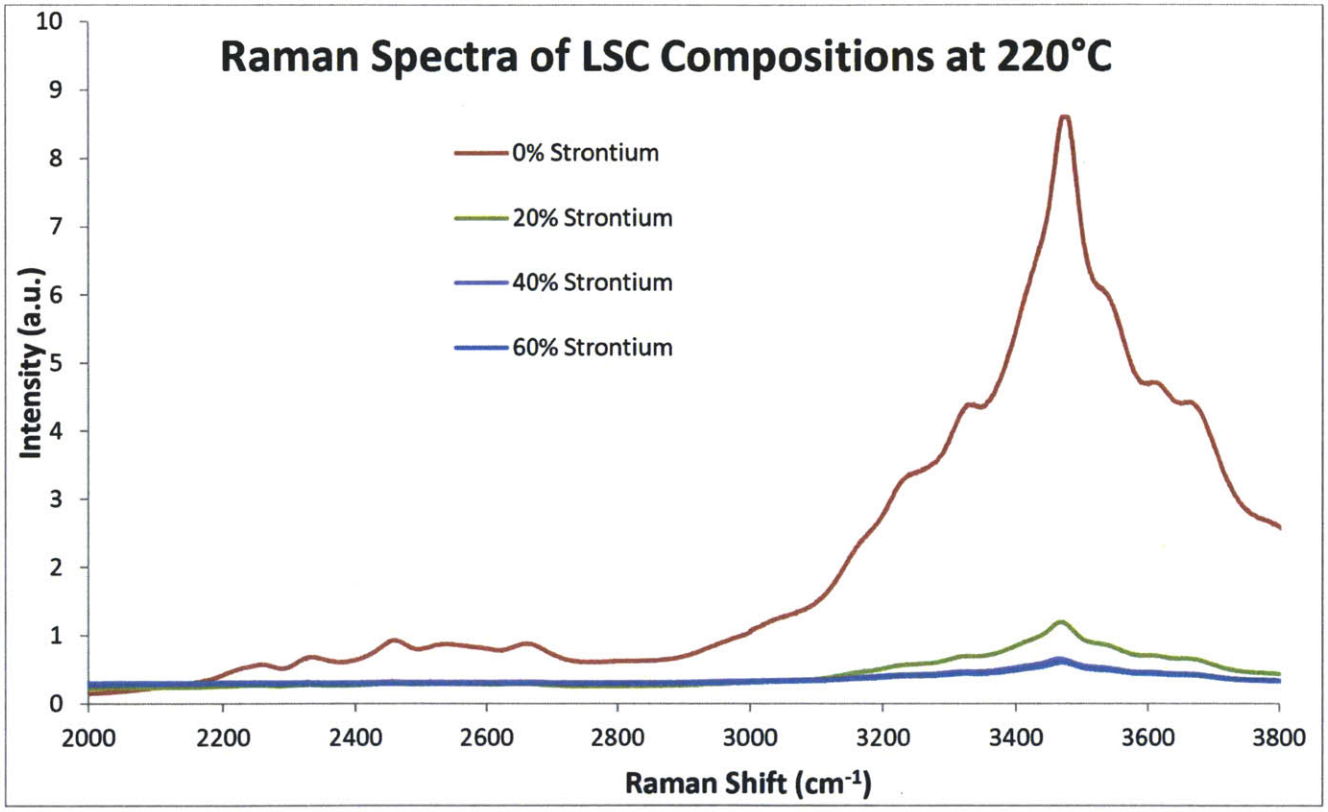

Fig. 8 Collected spectra at 220°C for 0% to 60% strontium compositions of LSC above 2000 cm^{-1}.

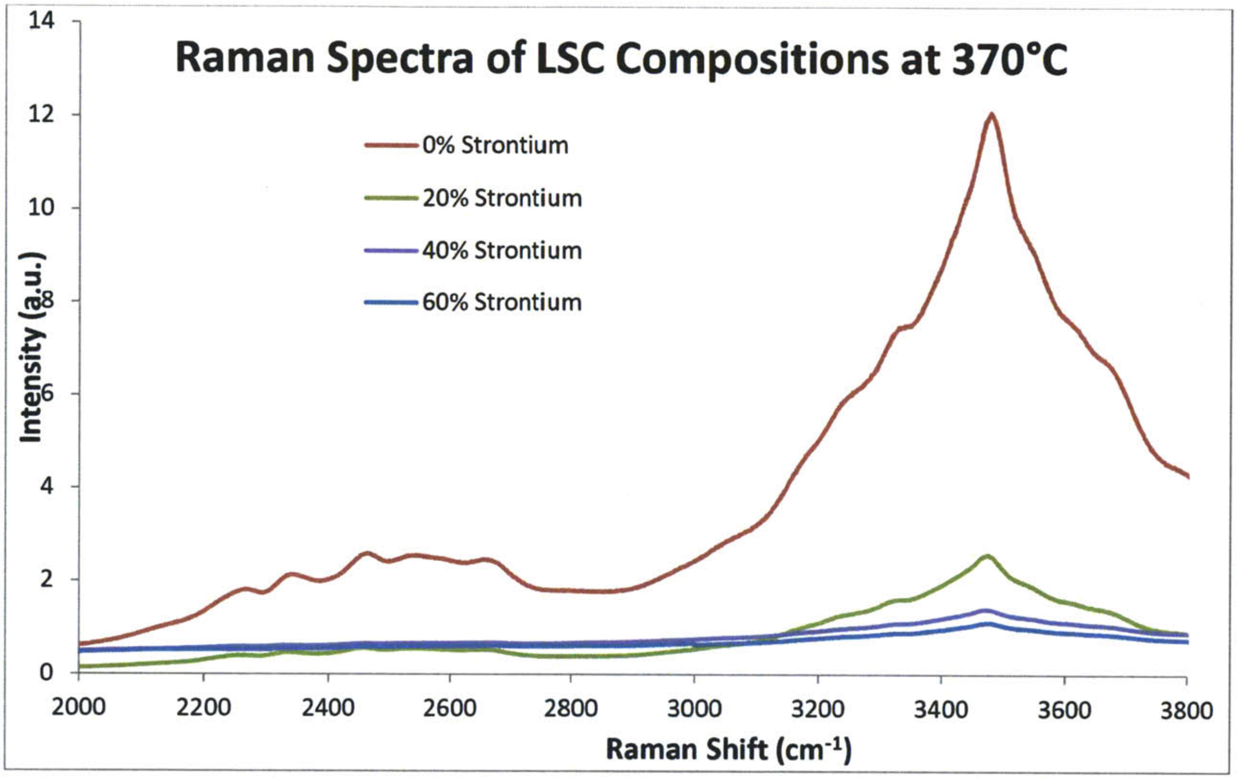

Fig. 9 Collected spectra at 370°C for 0% to 60% strontium compositions of LSC above 2000 cm-1.

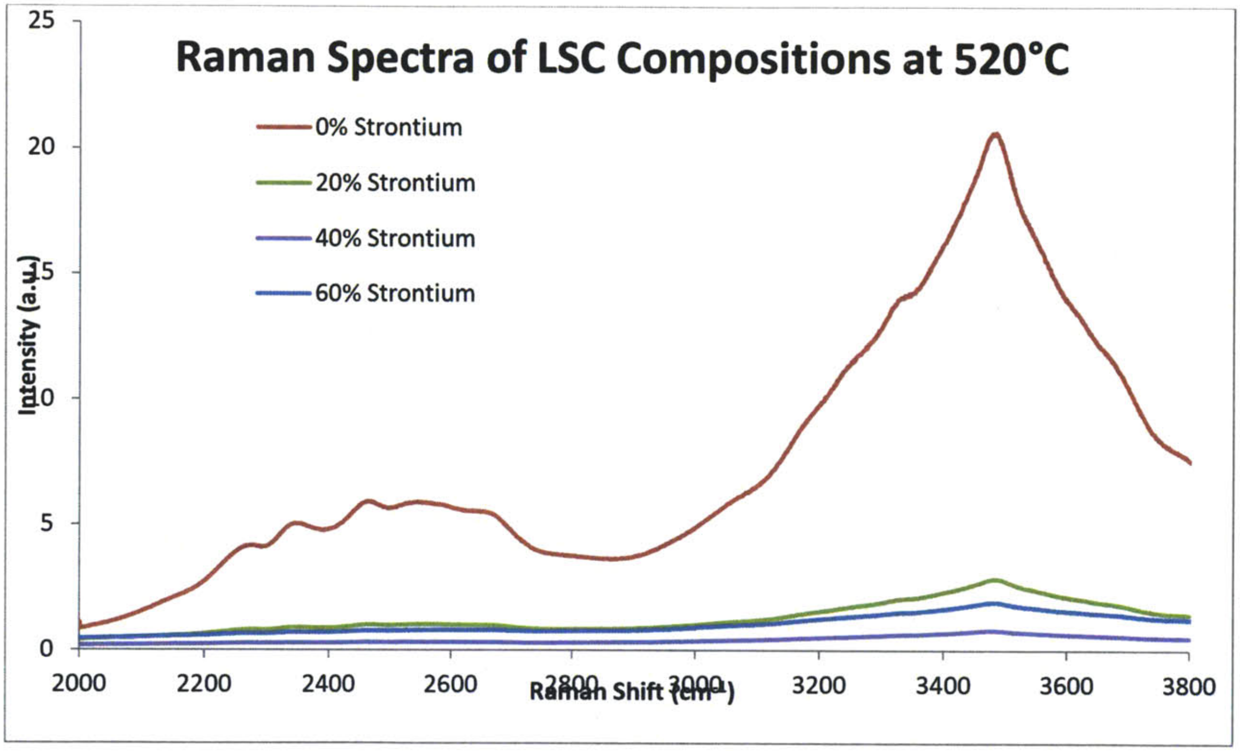

Fig. 10 Collected spectra at 520°C for 0% to 60% strontium compositions of LSC above 2000 cm-1.

3.4 Discussion – Surface Regime

The region above 1500 cm^{-1} relates to the polarizability tensors of surface specific structures or species as well as several organic complexes.[21] There are several identifiable structural peaks but the region above 2000 wavenumbers is more subtle: there are two general peak areas with different hypotheses for their presence.

The wide, sharp peak centered around 3300 wavenumbers is most likely a result of O-H bond response in all spectra (Fig. 7-10). The high intensity could be due to exposure of oxygen dangling bonds to humidity in the air, leading to a large number of hydroxide bonds at surface. Since the intensity is also proportional to the wavenumber, the usually Raman-weak response of O-H bonds may be heightened.

The other grouping of peaks from 2200 cm^{-1} to 2700 cm^{-1} is more open to speculation. The dulling of the peaks across strontium concentrations suggests a structural dependence similar to the structural wavenumber regime, where the peaks get less defined the higher the symmetry in the system is. Compare Fig. 10 to Fig. 7 to observe the stark temperature dependence of the response.

Another interesting factor is the temperature dependence, similar to what was seen in the YSZ-GDC samples, suggesting there may be a systematic reason for these peaks, perhaps due to the 10% O_2 environment.

One possibility is that they are surface termination effects with unique surface complexes forming on the material. These are not visible at room temperature so highly localized structural changes would be difficult to pick up. But a lack of thermal expansion shift of the peaks does not support this theory. Discussion on this set of peaks is mostly speculative since Raman studies of LSC past 230°C is completely novel.

3.5 Discussion – Comparison with Previous Work

Raman Mode	**Method**	**Frequency (cm^{-1})**	**Ref.**
E_g	Experimental	86	19
		104.8	8
		114	20
	DFT	82	20
E_g	Experimental	150	
		172	19
		177.4	8
		162	13
		204	20
	DFT	175.3	20
A_{1g}	Experimental	262	
		261	19
		287	20
	DFT	279.6	20
E_g	Experimental	413	
		432	19
		448	13
		488	20
	DFT	437	20
E_g	Experimental	590	
		583	19
		581	20
	DFT	600	20

Table 1. Comparison of results vs. other structural studies at lower than *in situ* temperatures as well as DFT calculations.

Peaks match well with other studies, both Inelastic Neutron Scattering (INS) and Raman studies, as well as proximity to DFT calculations of Raman modes. Table 1 compares experimental results versus other references. The mode at 86 cm^{-1} was not detected, most likely due to an incident light frequency filter placed on the detector to avoid damage to the instrument. Note that Raman peaks are generally closer to DFT peaks than INS, suggesting merit in further Raman studies.

Through previous work, the increase of k_q with higher concentrations of Strontium in LSC has been shown.[23] Increase of symmetry within the material is the only relation that can be made to electroimpedance spectroscopy (EIS) results from Mutoro et. al., although the damping of the surface regime may also be related. If surface data can be correlated to levels of oxygen nonstoichiometry, a stronger quantitative relationship may be formed.

3.6 Future Research

Due to the uncertainty in the high wavenumber regime, future work would be best served resolving that area. Temperature scans under different oxygen concentration conditions after a more rigorous surface cleaning could resolve the hydroxide peaks. Also, due to theorized structural changes during operation of the fuel cell, changes in the material may only be shown under full operating condition with a full fuel cell set up. A more elaborate experimental set up would then be useful to allow for simultaneous EIS for more direct correlation of structure to k^q. It has also been shown that varying oxygen concentration leads to different levels of non-stoichiometry within LSC.[24] For scans of areas with inconsistently appearing peaks (413 cm^{-1} Eg), polarizability scans may be used to properly correlate data. Intensities of peaks show a certain periodicity with rotation and peak assignments can be made through phase shift of these peaks.[25]

Other routes include investigating Surface Enhanced Raman Spectroscopy and also Tip Enhanced Raman Spectroscopy. These techniques have shown capabilities of peak amplification by placing metal nanoparticles on the surface. These nanoparticles increase Raman peak intensity by amplifying the local electromagnetic field. SERS effects have been shown with Ag, Au, and Cu.[26] Temperature runs with SERS have not been done however. Whether or not atom diffusion would change the surface structure of the material at higher temperatures would need to be resolved, most likely through XRD after a thermal cycling of the material.

Tip Enhanced Raman Spectroscopy (TERS) is another possibility. This is a technique that enhances electromagnetic fields of the sample similarly to SERS, however the metal does not make contact with the surface. The metal is formed into a tip that is brought close to the surface, but not touching. The enhancement is highly localized and resolution on the 10 nm range is possible.[27] Raman spectra of single molecules have been shown through TERS and high temperature, *in situ* set ups are exciting through this technique due to lack of foreign metal diffusion into the sample.

Lastly, Anti-Stokes measurements can be used. Due to the significantly lower Anti-Stokes response,[11] longer acquisition times can be used to resolve Raman peaks. Wide ranges are difficult to resolve, however, and background effects due to temperature in the Anti-Stokes regime is largely unknown.

4.0 Conclusion

In this thesis, I have applied a spectroscopy technique to probing the structural change of $La_{1-x}Sr_xCoO_{3-\delta}$ across change in composition and temperature. Through the use of Raman scattering spectroscopy, spectra showing Raman active vibrational modes and surface effects were shown over the range of 50 to 3800 cm^{-1}. Results were consistent with relevant data, but no transition to the high spin state was observed. While no structural phase changes were found in the research of this thesis, interesting effects in the surface regime were observed and possible explanations offered. Future research should focus on resolving the surface regime and consistent resolution of peaks.

Acknowledgements

I would like to thank Wesley Hong for all his help in understanding the complexities of Raman scattering and his guidance in my laboratory procedure. Also, I would like to thank my thesis advisor, Professor Shao-Horn, for advising me through this project, the Electrochemical Energy Lab for allowing me to share lab space with them, and the Department of Materials Science at MIT for teaching me throughout my four years here.

References

1. S Adler, *Chem. Rev.* (2004) **104**, 4791-4843
2. M Liu, M E Lynch, K Blinn, F M Alamgir, Y Choi, *Materials Today* (2011) **14**, 534-546
3. E Crumlin, E Mutoro, Sung-Jin Ahn, G J la O', D N Leonard, A Borisevich, M D Biegalski, H M Christen, Y Shao-Horn *J. Phys. Chem. Lett.*, (2010), **21**, 3149–3155
4. E Crumlin, E Mutoro, Z Liu, M Grass, M D Biegalski, Y L Lee, D Dane H Christen, H Bluhm, Y Shao-Horn, *Energy Environ. Sci.*, (2012) **5**,6081-6088
5. S Carter, A Selcuk, R J Chater, J Kajda, J A Kilner, B C H Steele, *Solid State Ionics* (1992) **53-56**, 597-604
6. J B Goodenough *Rep. Prof. Phys.* (2004) **67**, 1915-1993
7. Y Li, R Gemmen, X Liu, *J. Power Sources,* (2010) 195, 3345-3358
8. Y Kobayashi, Thant Sin Naing, M Suzuki, M Akimitsu, K Asai, *Physical Review B* (2005) **72**, 174405
9. M Yashima, T Tsuji J. Applied Crystallography (2007) **40**, 1166-1168
10. C Kittel, Introduction to Solid State Physics: Eighth Edition, John Wiley & Sons Ltd., Chichester, 2005
11. D A Long, The Raman Effect: A Unified Treatment of the Theory of Raman Scattering by Molecules, John Wiley & Sons Ltd., Chichester 2002
12. D Khomskiim, U Low (2003) Thesis, arXiv:cond-mat/0106135v2
13. N Orlovskaya, D Steinmetz, S Yarmolenko, D Pai, J Sankar, J Goodenough, *Physical Review B* (2005) **72**, 014122
14. Bilbao Crystallographic Server, http://www.cryst.ehu.es/ (accessed 2012)
15. E Wachsman, K Lee, Science (2011) **334**, 935-939
16. C Sun, R Hui, J Roller, *J Solid State Electrochem.,* (2010) **14**, 1125-1144
17. D Brett, A Atkinson, N Brandon, S Skinner, *Chem. Soc. Rev.*, (2008) **37**, 1568-1578
18. M B Pomfret, J C Owrutsky, R A Walker, *Annu. Rev. Anal. Chem.,* (2010) **3**, 151-174
19. A Ishikawa, J Hohara, S Sugai, *Physical Review Letters* (2004) **93**, 136401
20. N Golosova, D Kozlenko, A Kolesnikov, V Kazimirov, M Smirnov, *Physical Review B* (2011) **83**, 214305
21. Raman Data and Analysis, http://www.horiba.com/fileadmin/uploads/Scientific/Documents/Raman/bands.pdf
22. H Abernathy, PhD Dissertation (2008) Georgia Tech
23. E Mutoro, E Crumlin, M Biegalski, H Christen, Y Shao-Horn, *Energy Environ. Sci.*, (2011) **4**, 3689-3696
24. Lankhorst
25. D Tuschel, Spectroscopy (2012) **27**, 2-6
26. A Kudelski, *Surface Science* (2009) **603**, 1328-1334
27. H Xu, E Bjerneld, M Kall, L Borjsenn, *Physical Review Letters* (1999) **83**, 4357

Appendix A – Temperature Calibration

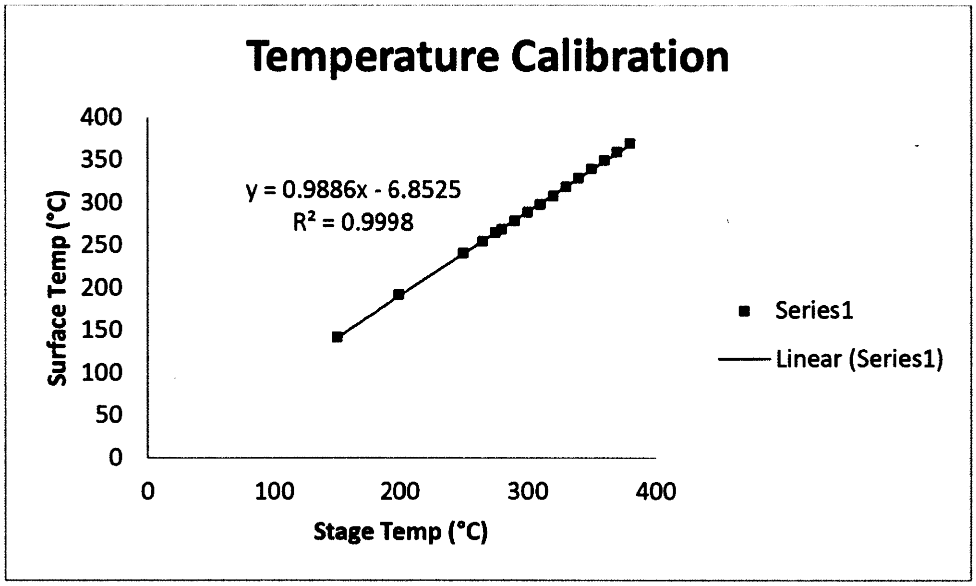

Fig. 11 Temperature comparison for proper experimental calibration

Linear equation form is consistent with a thin slab that has a flux boundary on one end (detected stage temperature) and a convective boundary on the other. By projection, at 530°C stage reading is equivalent to a 517°C surface temperature.

Appendix B – Full Spectra with Relative Intensities

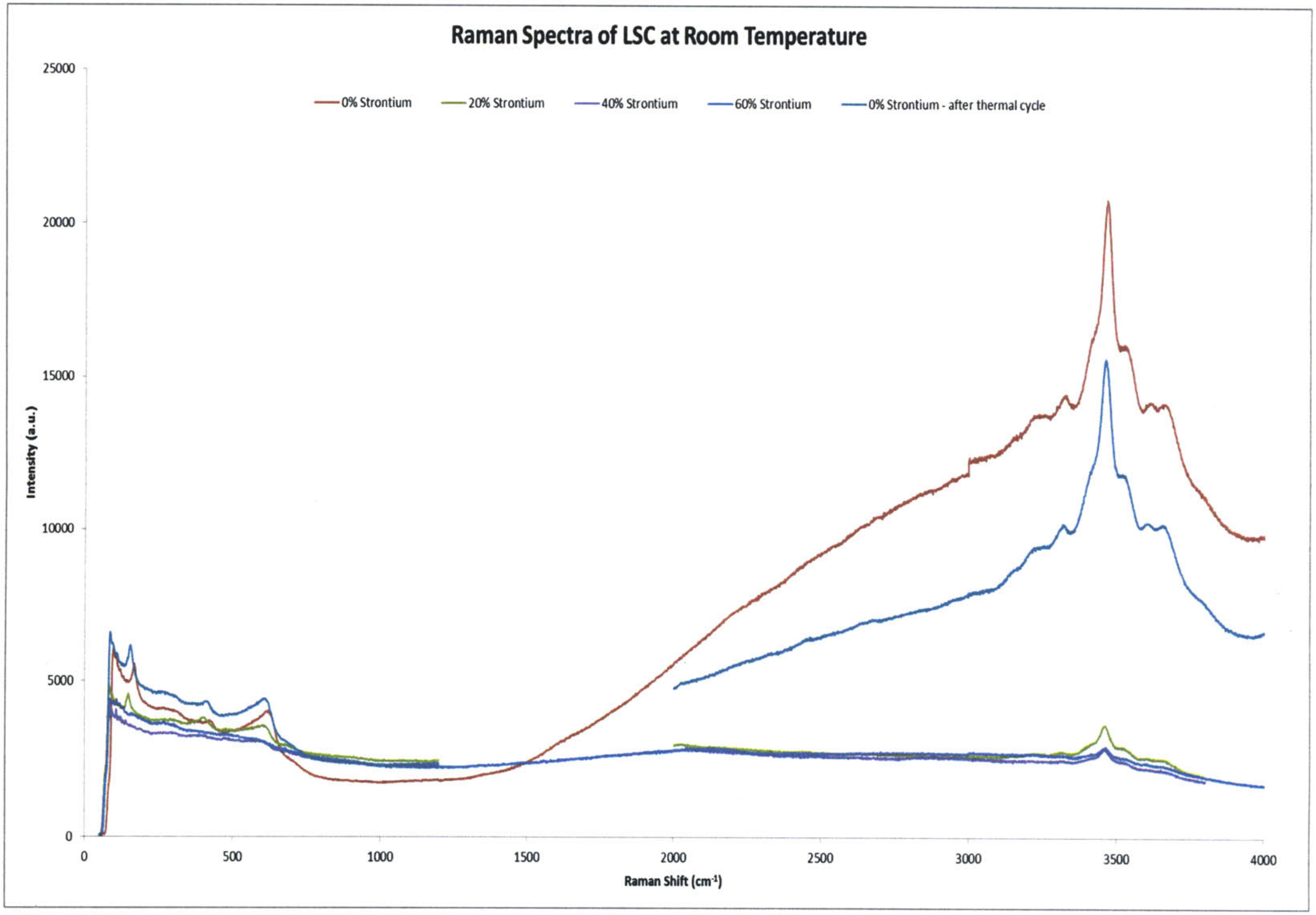

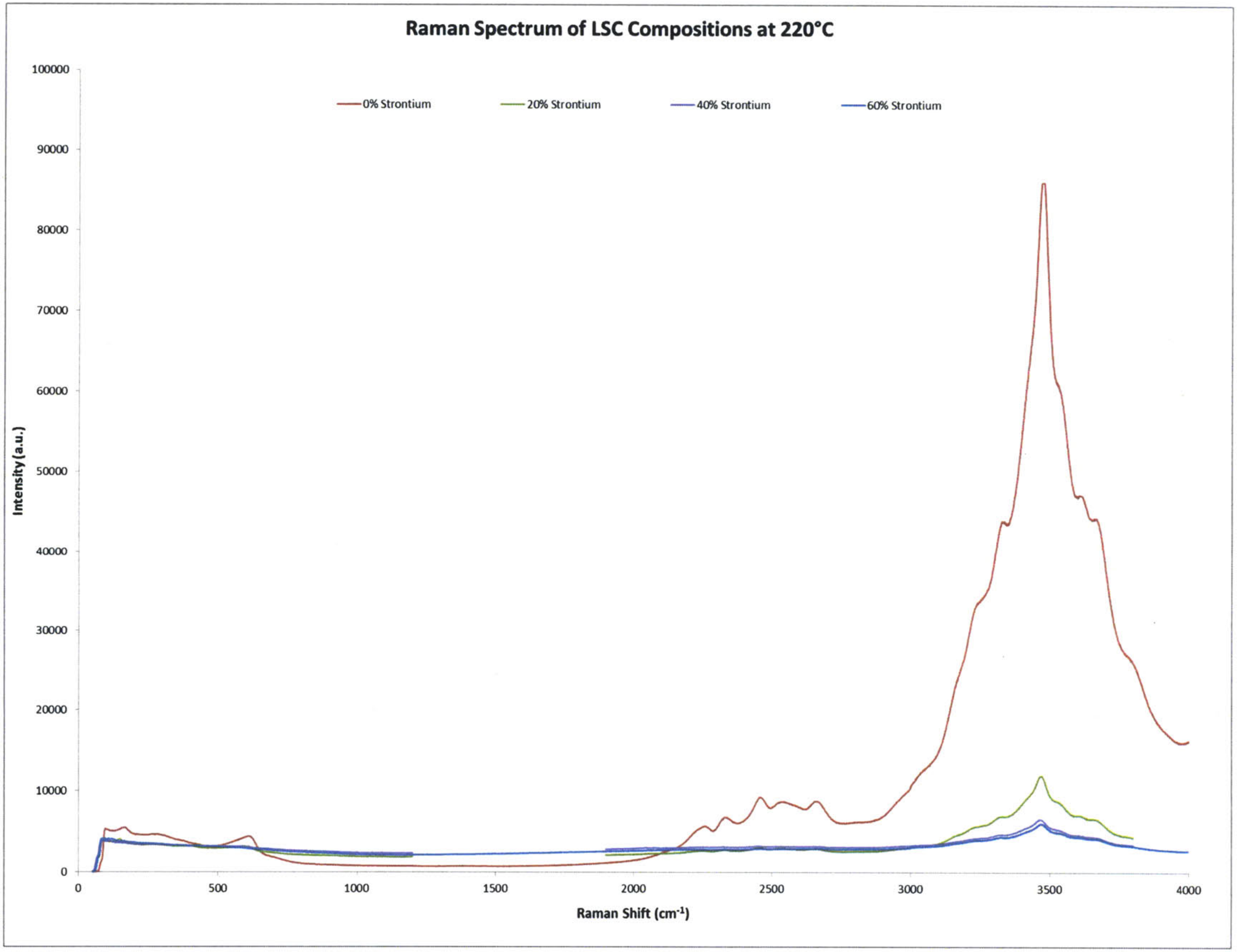
Raman Spectrum of LSC Compositions at 220°C
0% Strontium
20% Strontium
40% Strontium
60% Strontium
Intensity (a.u.)
100000
90000
80000
70000
60000
50000
40000
30000
20000
10000
0
0
500
1000
1500
2000
2500
3000
3500
4000
Raman Shift (cm-1)

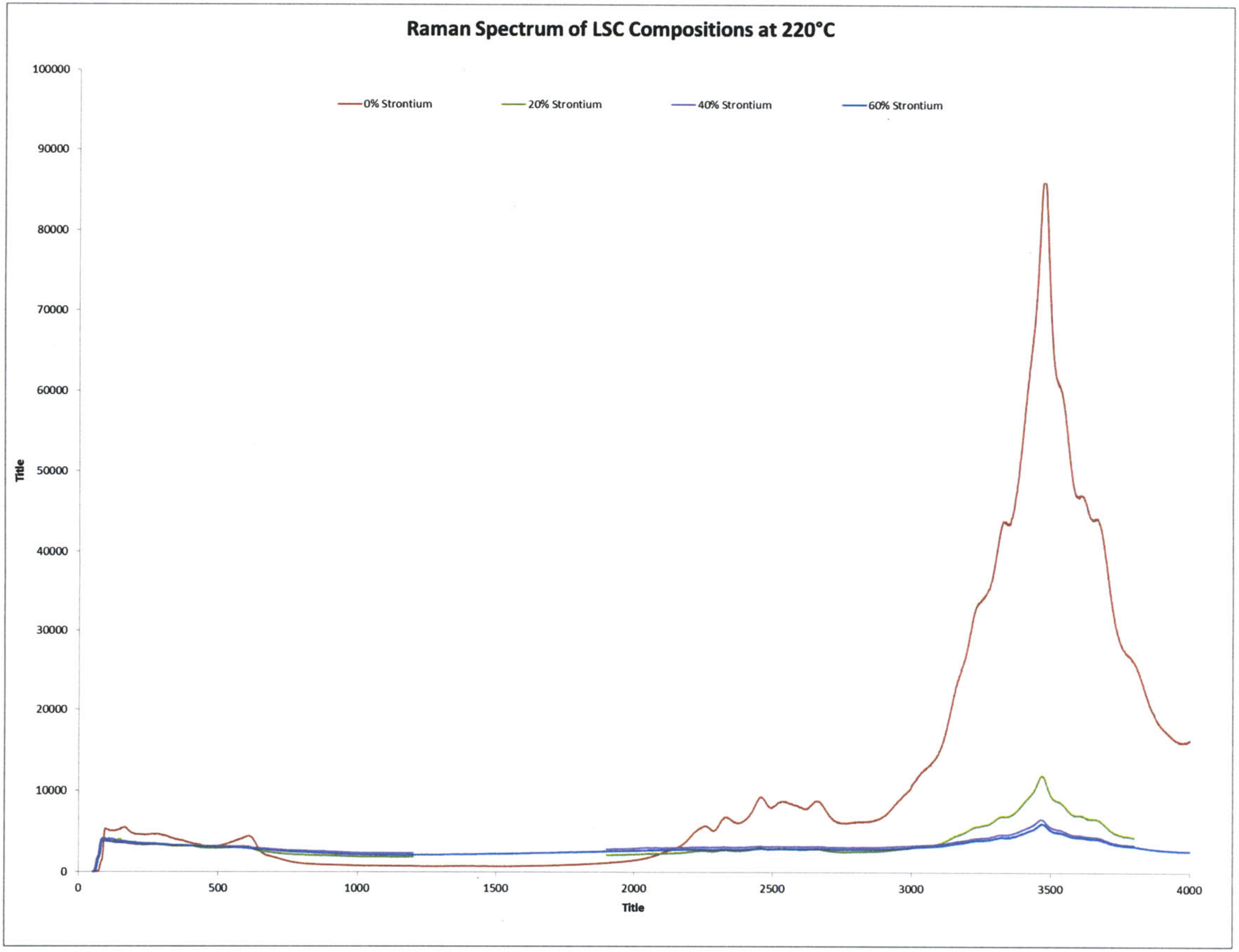
Raman Spectrum of LSC Compositions at 220°C
0% Strontium
20% Strontium
40% Strontium
60% Strontium
100000
90000
80000
70000
60000
50000
40000
30000
20000
10000
0
Title
0
500
1000
1500
2000
2500
3000
3500
4000
Title

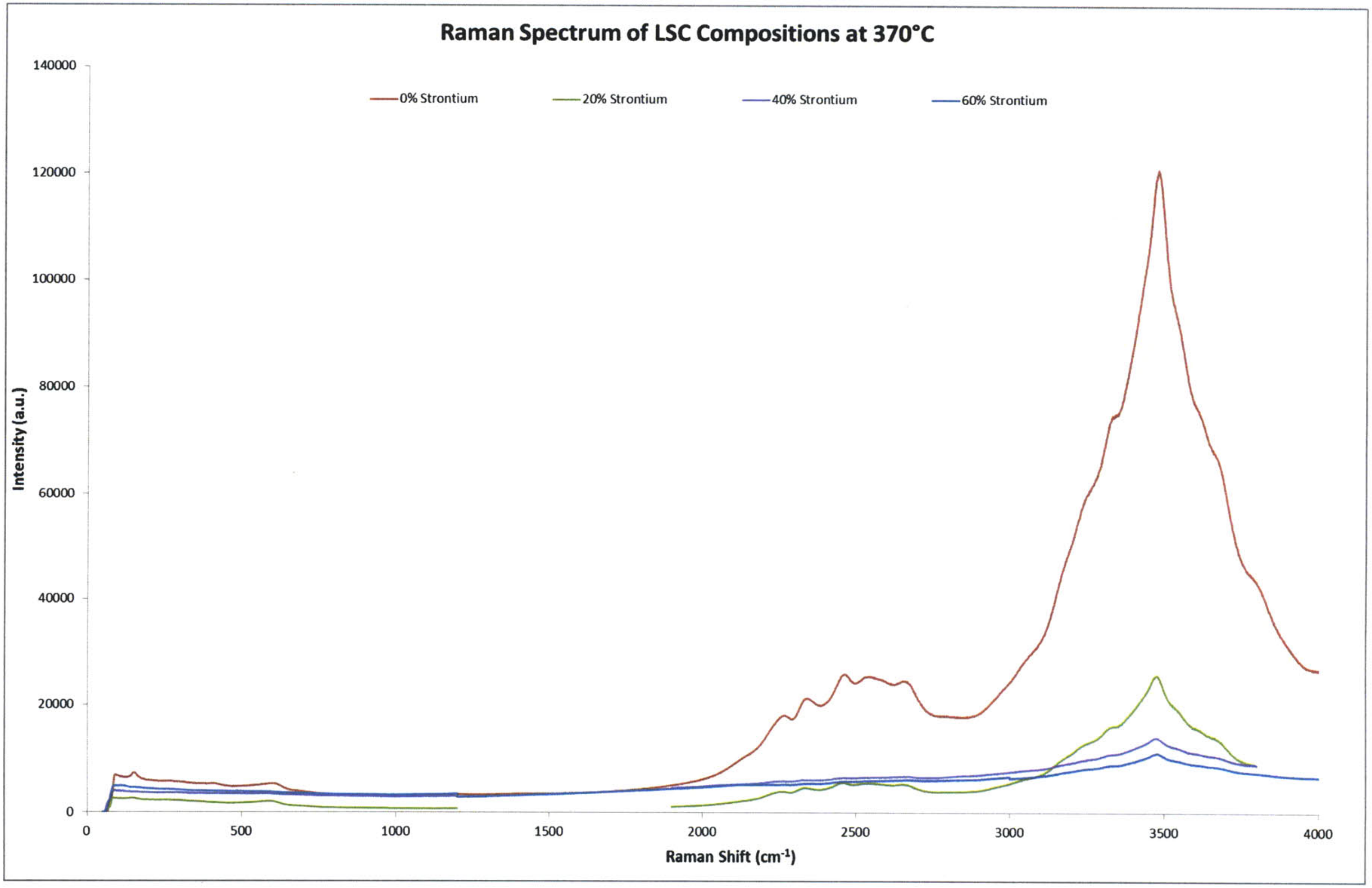
Raman Spectrum of LSC Compositions at 370°C
0% Strontium
20% Strontium
40% Strontium
60% Strontium
Intensity (a.u.)
140000
120000
100000
80000
60000
40000
20000
0
0
500
1000
1500
2000
2500
3000
3500
4000
Raman Shift (cm^{-1})

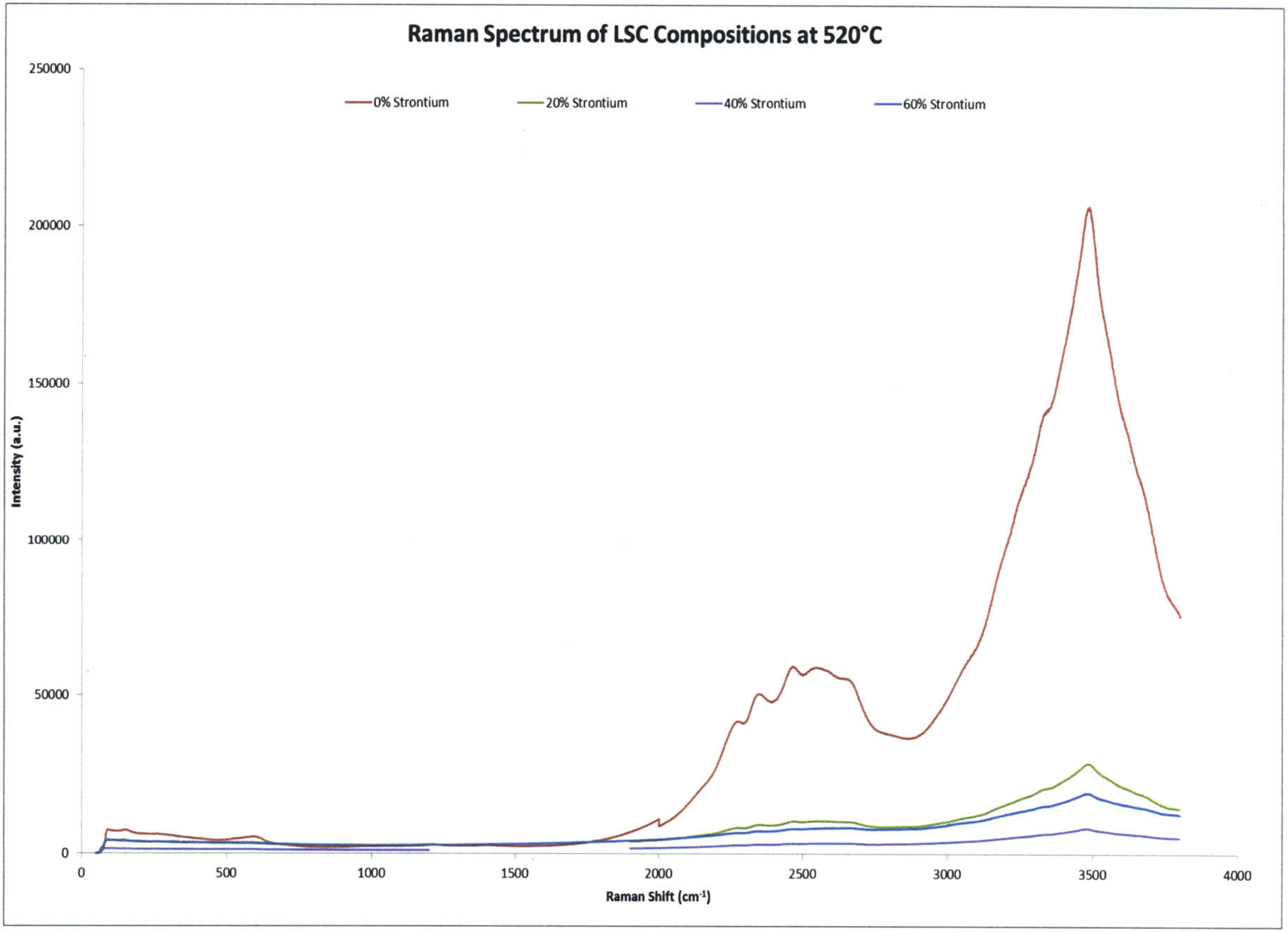
Raman Spectrum of LSC Compositions at 520°C
0% Strontium
20% Strontium
40% Strontium
60% Strontium
Intensity (a.u.)
250000
200000
150000
100000
50000
0
0
500
1000
1500
2000
2500
3000
3500
4000
Raman Shift (cm-1)

Appendix C – YSZ-GDC Base Spectra